



Redirecting dynamic surface restructuring of a layered transition metal oxide catalyst for superior water oxidation

Jian Wang¹✉, Se-Jun Kim², Jiapeng Liu³, Yang Gao⁴, Subin Choi¹, Jeongwoo Han¹, Hyeyoung Shin⁵, Sugeun Jo¹, Juwon Kim¹, Francesco Ciucci^{3,6}, Hwiho Kim¹, Qingtian Li⁷, Wanli Yang⁸, Xia Long⁸, Shihe Yang⁸✉, Sung-Pyo Cho⁹, Keun Hwa Chae¹⁰, Min Gyu Kim¹⁰, Hyungjun Kim²✉ and Jongwoo Lim¹✉

Rationally manipulating the in situ formed catalytically active surface of catalysts remains a tremendous challenge for a highly efficient water electrolysis. Here we present a cationic redox-tuning method to modulate in situ catalyst leaching and to redirect the dynamic surface restructuring of layered $\text{LiCoO}_{2-x}\text{Cl}_x$ ($x = 0, 0.1$ or 0.2), for the electrochemical oxygen evolution reaction (OER). Chlorine doping lowered the potential to trigger in situ cobalt oxidation and lithium leaching, which induced the surface of $\text{LiCoO}_{1.8}\text{Cl}_{0.2}$ to transform into a self-terminated amorphous (oxy)hydroxide phase during the OER. In contrast, Cl-free LiCoO_2 required higher electrochemical potentials to initiate the in situ surface reconstruction to spinel-type $\text{Li}_{1-x}\text{Co}_2\text{O}_4$ and longer cycles to stabilize it. Surface-restructured $\text{LiCoO}_{1.8}\text{Cl}_{0.2}$ outperformed many state-of-the-art OER catalysts and demonstrated remarkable stability. This work makes a stride in modulating surface restructuring and in designing superior OER electrocatalysts via manipulating the in situ catalyst leaching.

Water electrolysis, which currently accounts for 4% of the global hydrogen production, is expected to expand its share to 22% by 2050, as predicted by the International Energy Agency¹. The sluggish kinetics of the oxygen evolution reaction (OER) at the anode is among the most serious bottlenecks that restrict the power-to-gas efficiency and hinder the widespread application of water electrolyzers. Generally, transition metal oxides (TMOs) are more thermodynamically stable than metal sulfides, nitrides and phosphides under oxidative potentials². Several categories of non-precious TMOs have shown promising OER activities^{3,4}, and developing higher-performance OER electrocatalysts warrants establishing the actual structure–property–performance relationship^{5,6}. In this regard, several OER activity descriptors have been proposed, for example, $\text{OH}-\text{M}^{2+8}$ bond strength⁷, $\Delta G_{\text{O}^\cdot} - \Delta G_{\text{HO}^\cdot}$ (ref. ⁸), e_g orbital occupancy⁹ and the oxygen 2*p* band centre¹⁰. However, the evolution of structural and physicochemical properties of catalysts during electrocatalysis complicates the use of the above-mentioned descriptors to predict the OER, especially when phase transformation and surface restructuring occur during water electrolysis^{11,12}. Tracking the structural evolution of catalysts and elucidating the nature of catalytically active surfaces remain difficult^{13–15}. Further modulating the dynamic surface restructuring and manipulating the in situ generated active surface species are even more challenging. Recent work found that metal (hydro)oxide catalysts underwent

in situ leaching of cations^{16,17} or anions¹⁸ during the OER, which defined the newly formed active surface. However, precisely modulating the in situ leaching has seldom been realized, which prevents a superior control of the restructured active surface.

A model material for investigating redox-related OER activity is layered LiCoO_2 . The arrangement of transition metals in LiCoO_2 (edge-sharing octahedral) is different to those of perovskite-type TMOs^{19,20} and spinel-type TMOs^{21,22}, but mimics those of highly active layered transition metal (oxy)hydroxides^{23–25}. However, layered LiCoO_2 is inert for OER catalysis^{26,27}, and even inferior to its spinel counterpart^{27,28}. Cui and co-workers pioneered the ex situ electrochemical method in which the Li composition of the layered LiCoO_2 is tuned in an organic battery electrolyte before demonstrating an improved oxygen electrolysis in aqueous solutions^{29,30}. Although one can predict that delithiated $\text{Li}_{1-x}\text{CoO}_2$ ($x \sim 0.5$) thermodynamically undergoes a phase transition from the layered structure to the cubic spinel-type $\text{Li}_{1-x}\text{Co}_2\text{O}_4$ (refs. ^{31,32}), dynamic restructuring of $\text{Li}_{1-x}\text{CoO}_2$ during the OER was not monitored³³. In addition, engineering or even bypassing this thermodynamically predicted phase in situ for layered LiCoO_2 to achieve high electrocatalytic activities has seldom been realized.

Here we demonstrate the application of cationic redox tuning in engineering the in situ leaching potential, manipulating the cation leaching amount and redirecting the dynamic surface restructuring

¹Department of Chemistry, College of Science, Seoul National University, Seoul, Republic of Korea. ²Department of Chemistry, Korea Advanced Institute of Science and Technology, Daejeon, Republic of Korea. ³Department of Mechanical and Aerospace Engineering, The Hong Kong University of Science and Technology, Hong Kong, China. ⁴College of Materials Science and Engineering, Hunan University, Changsha, China. ⁵Graduate School of Energy Science and Technology (GEST), Chungnam National University, Daejeon, Republic of Korea. ⁶Department of Chemical and Biological Engineering, The Hong Kong University of Science and Technology, Hong Kong, China. ⁷Advanced Light Source, Lawrence Berkeley National Laboratory, Berkeley, CA, USA. ⁸Guangdong Provincial Key Lab of Nano-Micro Material Research, School of Chemical Biology and Biotechnology, Peking University Shenzhen Graduate School, Shenzhen, China. ⁹National Center for Inter-University Research Facilities, Seoul National University, Seoul, Republic of Korea. ¹⁰Beamline Research Division, Pohang Accelerator Laboratory, Pohang University of Science and Technology, Pohang, Republic of Korea. ✉e-mail: jwangbx@connect.ust.hk; chsyan@pku.edu.cn; linus16@kaist.ac.kr; jwlim@snu.ac.kr

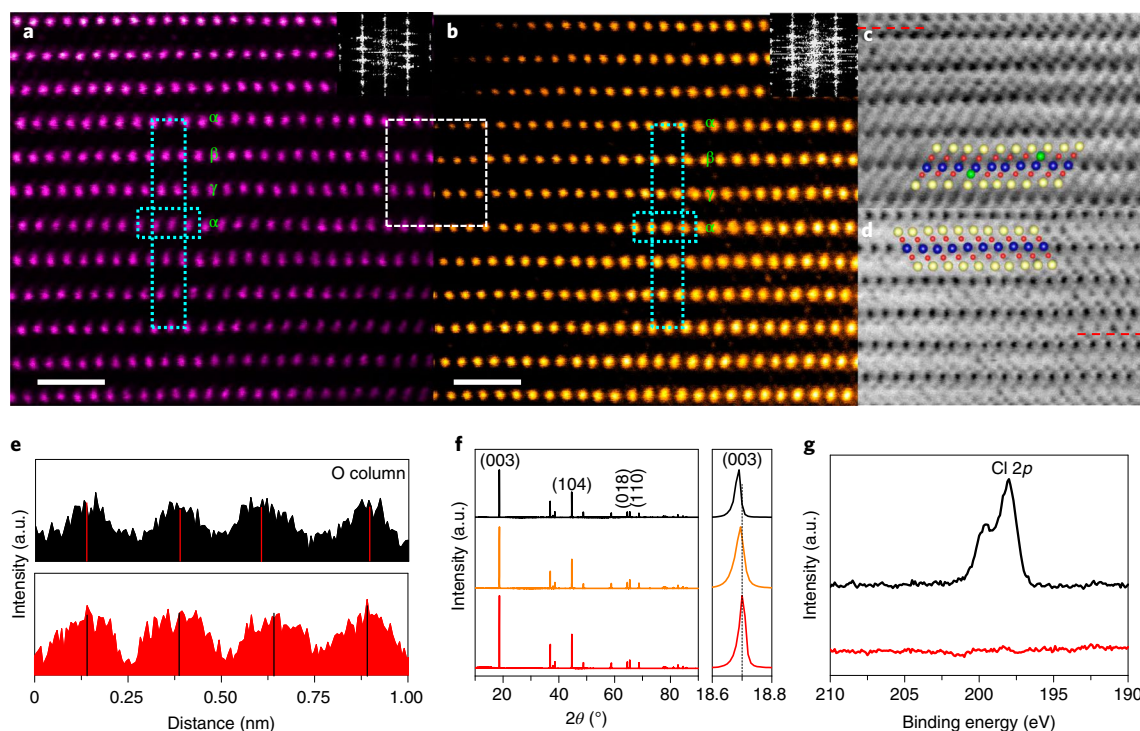


Fig. 1 | Structural and compositional characterizations. **a, b**, HAADF-STEM images of $\text{LiCoO}_{1.8}\text{Cl}_{0.2}$ (**a**) and LiCoO_2 (**b**). Insets: the corresponding FFT patterns at the [010] zone axis. Scale bars, 1 nm. **c, d**, Bright-field STEM images of $\text{LiCoO}_{1.8}\text{Cl}_{0.2}$ (**c**) and LiCoO_2 (**d**) at the [010] zone axis. The yellow, blue and red dots represent Li, Co and O atoms, respectively. The green dots represent Cl atoms for guidance only and do not represent the exact locations. **e**, Intensity line profile of the oxygen column extracted along the red line in **c** for $\text{LiCoO}_{1.8}\text{Cl}_{0.2}$ (top) and that in **d** for LiCoO_2 (bottom): peaks and valleys represent oxygen atoms and gaps, respectively. **f**, Synchrotron-based XRD patterns for $\text{LiCoO}_{1.8}\text{Cl}_{0.2}$ (top), $\text{LiCoO}_{1.9}\text{Cl}_{0.1}$ (middle) and LiCoO_2 (bottom) with the calibrated wavelength equal to 1.5226 Å. **g**, Cl 2p XPS for $\text{LiCoO}_{1.8}\text{Cl}_{0.2}$ (black) and LiCoO_2 (red). a.u., arbitrary units.

of layered LiCoO_2 under water oxidation. The electronic structure of LiCoO_2 is engineered by Cl substitution, which lowers the electrochemical potential to trigger in situ Co oxidation and delithiation during the OER. With a facile lithium extraction, the $\text{LiCoO}_{1.8}\text{Cl}_{0.2}$ surface forms a Cl-doped cobalt (oxy)hydroxide phase. In sharp contrast, Cl-free LiCoO_2 requires a larger electrochemical potential to initiate and a greater number of cycles to complete the surface restructuring into spinel-type $\text{Li}_{1+x}\text{Co}_2\text{O}_4$, resulting in an inferior OER catalytic performance.

Results

Structure and composition. $\text{LiCoO}_{2-x}\text{Cl}_x$ ($x=0, 0.1$ or 0.2) was prepared by a solid-state reaction method, for which the morphological and compositional information is provided in Supplementary Figs. 1 and 2 and Supplementary Table 1. After high-temperature calcination, the Cl-doped LiCoO_2 showed a high degree of crystallinity: sharp particle edges were visible, and the surface atom distribution was orderly (Supplementary Fig. 3). For the O3-type LiCoO_2 , the cobalt ions are ordered in an $\alpha\beta\gamma\alpha\beta\gamma$ stacking mode³⁴, which is well-demonstrated from the high-angle annular dark-field scanning transmission electron microscopy (HAADF-STEM) image in Fig. 1b. This type of $\alpha\beta\gamma\alpha\beta\gamma$ stacking was generally maintained for $\text{LiCoO}_{1.8}\text{Cl}_{0.2}$ (Fig. 1a), as supported by the similar fast Fourier transform (FFT) patterns in the inset. Nevertheless, slight displacements of the Co ions from the regular sites were detected (highlighted by the cyan-coloured rectangles in Fig. 1a,b), which might be related to the Cl dopants that form defects inside the LiCoO_2 lattice. The arrangement of light atoms, which included 3b-site Li and 6c-site O columns, can be distinguished from the bright-field STEM images in Fig. 1c,d ($\text{LiCoO}_{1.8}\text{Cl}_{0.2}$ and LiCoO_2 , respectively). The intensity line profiles of the oxygen column (Fig. 1e) demonstrate the

obvious difference: the generally uniform interatomic distance of oxygen atoms for LiCoO_2 and the uneven arrangement of oxygen site atoms in $\text{LiCoO}_{1.8}\text{Cl}_{0.2}$. Atom redistribution possibly occurs after Cl introduction to minimize the lattice energy.

$\text{LiCoO}_{1.8}\text{Cl}_{0.2}$ was characterized by a larger Co–O slab distance, as shown in the white-coloured rectangle in Fig. 1a,b and by the line profile comparison (Supplementary Fig. 4). This suggested a larger *c*-axis lattice parameter, which was supported by the negative shift of the (003) peak for Cl-doped LiCoO_2 in the X-ray diffraction (XRD) pattern (Fig. 1f). Cl^- is larger in size than O^{2-} , which potentially leads to the lattice expansion. The Rietveld refinement (Supplementary Fig. 5 and Supplementary Tables 2–4) confirmed that Cl-doped and pristine LiCoO_2 had the same $\alpha\text{-NaFeO}_2$ type structure ($R\bar{3}m$). The obvious split of the (018)/(110) peak in the XRD pattern indicates the high crystallinity of the as-prepared materials with few antites between the Li and Co ions³⁴. Further increasing the Cl dopant amount beyond 0.2 (that is, $x=0.25, 0.3$ and 0.5 in $\text{LiCoO}_{2-x}\text{Cl}_x$) generated minor impure phases (Supplementary Fig. 6). In contrast to LiCoO_2 , the presence of a Cl 2p peak in the X-ray photoelectron spectroscopy (XPS) profile of $\text{LiCoO}_{1.8}\text{Cl}_{0.2}$ (Fig. 1g) indicated that Cl was introduced. Furthermore, the energy-dispersive X-ray spectroscopy (EDS) mapping of the STEM image revealed a relatively homogeneous distribution of Co, O and Cl atoms in $\text{LiCoO}_{1.8}\text{Cl}_{0.2}$ (Supplementary Fig. 7).

Electronic configuration. Density functional theory (DFT) calculations and X-ray absorption spectroscopy (XAS) analyses were conducted to obtain theoretical and experimental insights into the electronic structures. DFT-optimized structures for $\text{LiCoO}_{2-x}\text{Cl}_x$ are illustrated in Fig. 2a. From the total and projected density of states (PDOS) (Fig. 2b), aliovalent Cl doping upwardly shifted the Fermi

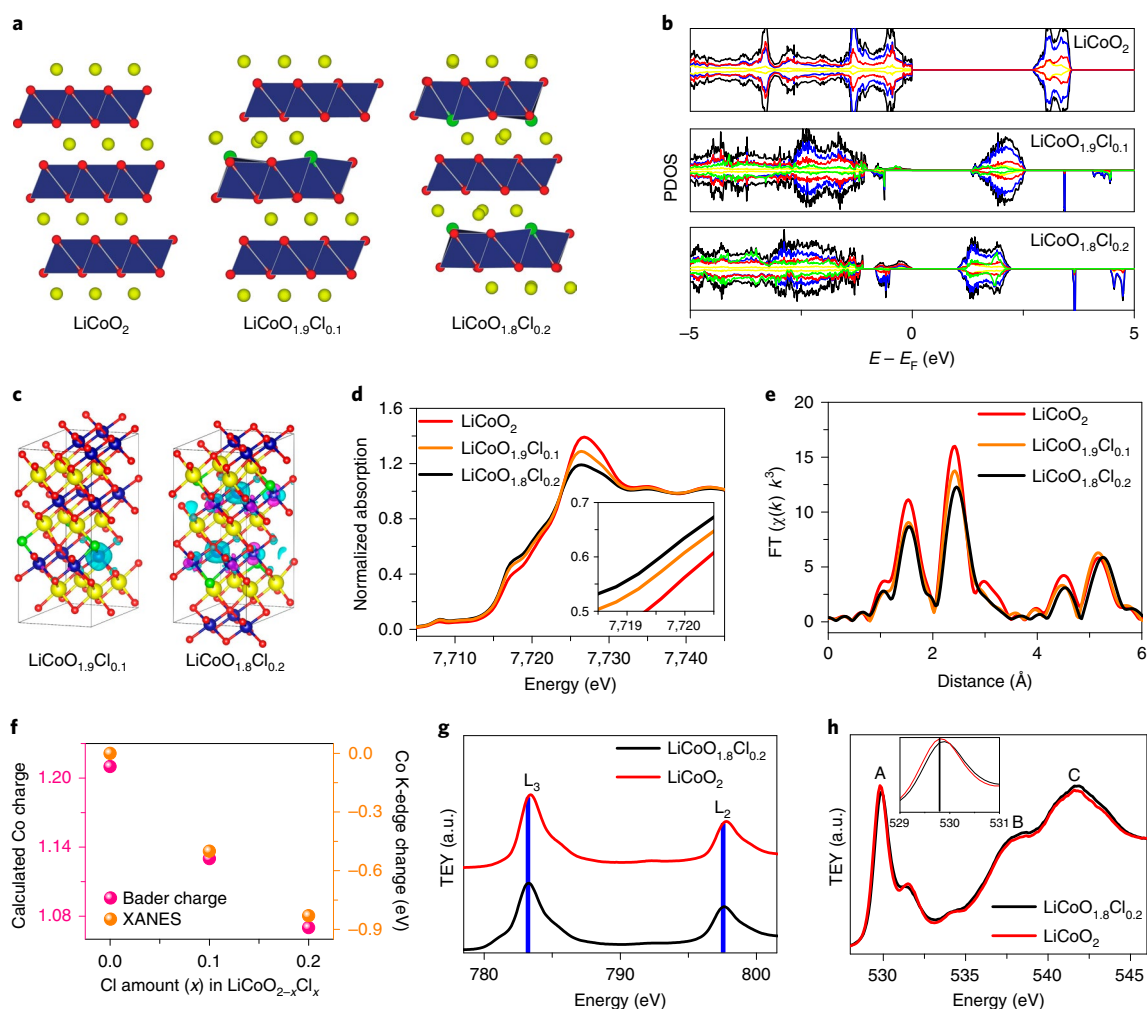


Fig. 2 | Electronic configuration. **a**, DFT-optimized atomic structures. Li, yellow; Co, blue; O, red; Cl, green. **b**, Total (black) and PDOS of Li (yellow), Co (blue), O (red) and Cl (green). The PDOS of Li and Cl are 20-fold magnified. **c**, Spin density of $\text{LiCoO}_{1.9}\text{Cl}_{0.1}$ and $\text{LiCoO}_{1.8}\text{Cl}_{0.2}$, with cyan and purple representing spin-up and spin-down electrons, respectively. The isovalue is set as 0.01 e bohr^{-3} . **d**, Normalized Co K-edge XANES spectra. **e**, Fourier-transformed (FT) k^3 -weighted Co K-edge EXAFS spectra. **f**, Co Bader charge of $\text{LiCoO}_{2-x}\text{Cl}_x$ ($x = 0, 0.1$ or 0.2) and their Co K-edge shift relative to that of LiCoO_2 . **g**, Co L-edge sXAS. **h**, O K-edge sXAS.

level closer to the conduction band edge, and the gap between the valence band maximum and the conduction band minimum was reduced from 2.7 eV for LiCoO_2 to 1.3 and 1.0 eV for $\text{LiCoO}_{1.9}\text{Cl}_{0.1}$ and $\text{LiCoO}_{1.8}\text{Cl}_{0.2}$, respectively. This suggests a beneficial effect of Cl doping for enhanced electrical conductivity³⁵, which ascribes to the reduced charge transfer resistance (vide infra). More details of the electronic band structures and band-decomposed charge density distributions are provided in Supplementary Fig. 8. The spin density shown in Fig. 2c is mostly localized on the Co atom nearby the doped Cl, which clearly indicates that the Cl doping reduces the Co^{3+} ($S = 0$) to Co^{2+} ($S = 1/2$).

Even though the calculated Bader charge was lower than the nominal value³⁶, the trend was clear that a greater Cl doping amount reduced the valence state of Co in $\text{LiCoO}_{2-x}\text{Cl}_x$ (Fig. 2f). Replacement of O^{2-} with Cl^- yielded a Co valence state of less than +3, as validated by the negative shift of the absorption edge position in the normalized Co K-edge X-ray absorption near edge structure (XANES) spectra for $\text{LiCoO}_{1.9}\text{Cl}_{0.1}$ (by 0.50 eV) and $\text{LiCoO}_{1.8}\text{Cl}_{0.2}$ (by 0.82 eV) relative to that of LiCoO_2 (Fig. 2d). This leftward shift corroborates the valence state decrease of the Co cations³⁷. Two major peaks were observed in the Fourier-transformed k^3 -weighted Co K-edge extended X-ray absorption fine structure

(EXAFS) spectra (Fig. 2e), which represents the neighbouring atomic shells in the vicinity of Co. The first peak around 1.5 Å could be ascribed to and best fitted with a Co–O/Cl coordination (Supplementary Fig. 9 and Supplementary Table 5), whereas the second major peak located around 2.5 Å, corresponded to the Co–Co coordination³⁸. Both $\text{LiCoO}_{1.9}\text{Cl}_{0.1}$ and $\text{LiCoO}_{1.8}\text{Cl}_{0.2}$ had a lower fitted Co–O/Cl coordination number than that of LiCoO_2 , which suggests an unsaturated Co environment. The fitted Co–Co distance (2.83 Å) matched the length of the two neighbouring Co ions for the edge-sharing octahedron in the layered LiCoO_2 . The Cl-doping-induced electronic structural change is also reflected by the redshift of the Raman spectrum (Supplementary Fig. 10).

In addition to the X-ray absorption fine structure (XAFS) providing the average bulk and surface information, the near-surface electronic structure was assessed by soft XAS (sXAS) with a total-electron-yield (TEY) signal. Two main peaks were observed in the Co L-edge sXAS profile (Fig. 2g), which were ascribed to the transitions of Co $2p_{3/2}$ (L_3 edge) and $2p_{1/2}$ core (L_2 edge) electrons to an unoccupied $3d$ orbital hybridized with an oxygen $2p$ orbital³⁹. In comparison to pristine LiCoO_2 , the Co $L_{2,3}$ edge of $\text{LiCoO}_{1.8}\text{Cl}_{0.2}$ shifted towards the lower energy regions by ~ 0.2 eV, which suggests that the valence state of surface Co remained lower than that

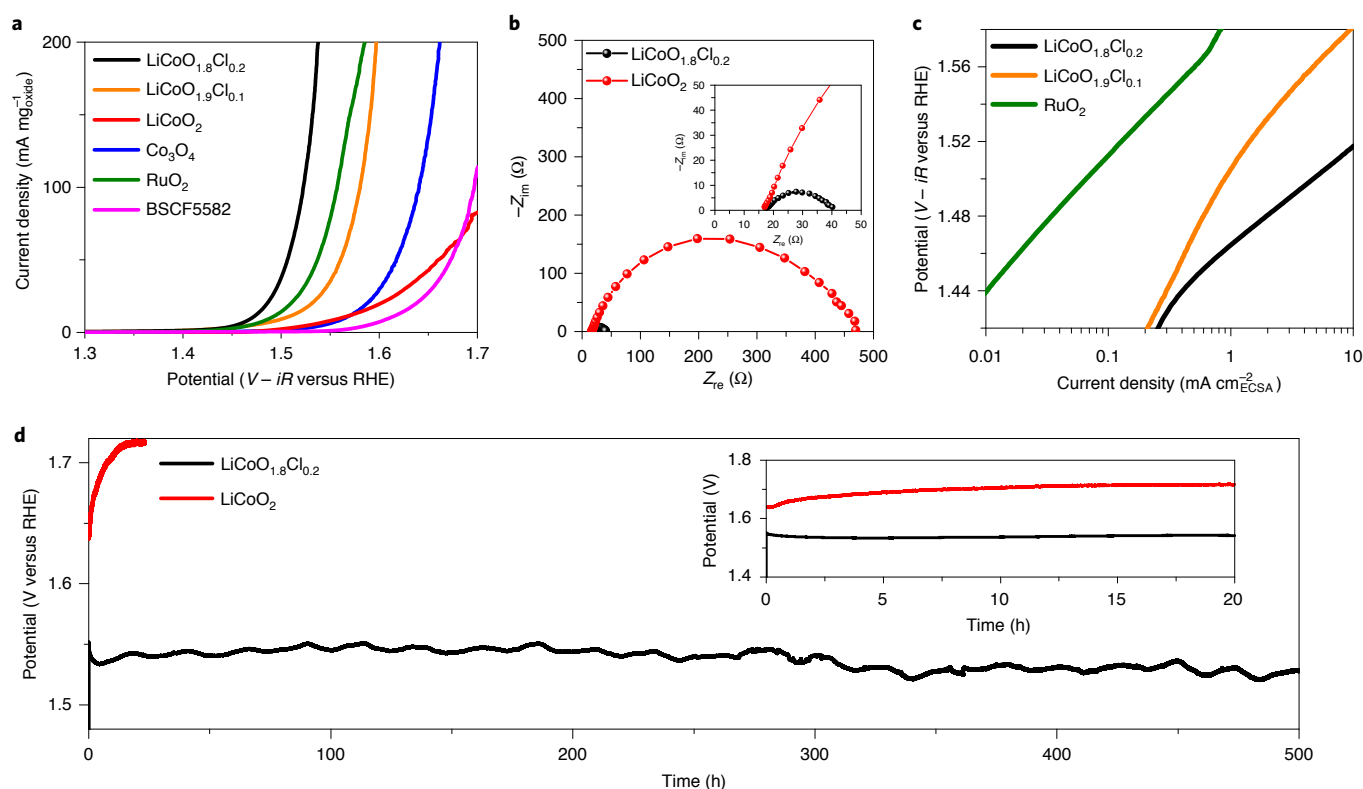


Fig. 3 | OER performance in 1M KOH. a, Mass activity. **b**, Electrochemical impedance spectroscopy at a positive potential of 1.55 V versus RHE. **c**, Specific activity. **d**, Chronopotentiometry test at 20 mA cm⁻².

of LiCoO₂ (+3). Three main peaks were detected in the O K-edge sXAS: an intense absorption peak at 530 eV (marked as peak A in Fig. 2h) and two broad peaks (B and C) above 536 eV. Peak A represents the transition of the O 1s electron to the hole state in the O 2p orbital hybridized with the Co 3d orbital, whereas the broad higher-energy peaks B and C are assigned to the transitions to the hybridized states of O 2p and Co 4sp orbitals^{39,40}. The shapes of the O K-edge sXAS were similar to those for LiCoO₂ and LiCoO_{1.8}Cl_{0.2}, and there was no obvious formation of an additional shoulder peak after Cl doping into LiCoO₂. Peak A for LiCoO_{1.8}Cl_{0.2} was found to slightly move to higher energy regions relative to that of LiCoO₂ (Fig. 2h inset), which might be due to the reduced Co, which is hybridized with O (refs. ^{39,40}).

Catalytic performance. With calibrating the potential of the reference electrode and precluding its potential drift (Supplementary Fig. 11), we recorded the cyclic voltammograms between 1.2 and 1.6 V versus the reversible hydrogen electrode (RHE). During the scans, LiCoO_{1.8}Cl_{0.2} was activated, in contrast to LiCoO₂, which underwent little change (Supplementary Fig. 12). Next, linear sweep voltammetry was performed with the current normalized by the disk area of the glassy carbon (GC), oxide mass, Brunauer–Emmett–Teller surface area (Supplementary Fig. 13), and electrochemical active surface area (Supplementary Note 1, Supplementary Fig. 14 and Supplementary Table 6), respectively. The OER activity increased notably with the Cl content, following the order LiCoO₂ < LiCoO_{1.9}Cl_{0.1} < LiCoO_{1.8}Cl_{0.2}. The charge-transfer resistance of LiCoO_{1.8}Cl_{0.2} (15.8 Ω) was also substantially reduced in comparison to that of pristine LiCoO₂ (315 Ω; see the electrochemical impedance spectroscopy and the fittings in Fig. 3b, Supplementary Fig. 15 and Supplementary Table 7). The generated gas products catalysed by LiCoO_{1.8}Cl_{0.2} were directly examined by the differential electrochemical mass spectrometry, which detected the target

O₂ gases and no obvious evolution of other impure gases during the OER (Supplementary Note 2 and Supplementary Fig. 16a,b). The potential leaching of Cl into the electrolyte during the OER was precluded by the AgNO₃ titration experiment (Supplementary Fig. 16c). The rotating ring-disk electrode test (Supplementary Note 3 and Supplementary Fig. 17) further confirmed that LiCoO_{1.8}Cl_{0.2} catalysed the OER with a high Faradaic efficiency, and its large OER current density was mainly ascribed to the desired 4e⁻ pathway (4OH⁻ → O₂ + 2H₂O + 4e⁻) rather than the 2e⁻ peroxide formation (2OH⁻ → H₂O₂ + 2e⁻). LiCoO_{1.8}Cl_{0.2} outperformed the benchmark RuO₂, perovskite-type Ba_{0.5}Sr_{0.5}Co_{0.8}Fe_{0.2}O_{3-δ} (BSCF5582) and spinel-type Co₃O₄ (Fig. 3a). In particular, the specific activity of LiCoO_{1.8}Cl_{0.2} (Fig. 3c) and Supplementary Fig. 18) was about two orders of magnitude higher than that of RuO₂, which demonstrates its great potential in catalysing the OER. It is also worth noting that LiCoO_{1.8}Cl_{0.2} required a small overpotential of 290 mV to deliver a current density of 200 mA mg_{oxide}⁻¹ (Fig. 3a) and 302 mV for 50 mA cm_{geo}⁻² (where ‘geo’ is the disk geometry area; Supplementary Fig. 19), comparable or superior to those of many state-of-the-art OER electrocatalysts (Supplementary Table 8). Remarkably, LiCoO_{1.8}Cl_{0.2} had an excellent durability for 500 hours without obvious degradation (Fig. 3d). In contrast, consistent with previous reports^{27,33}, layered LiCoO₂ required increased overpotentials to sustain the high current density.

Dynamic cobalt redox. To explore how Cl doping substantially boosted the OER activity of LiCoO₂, operando XAFS spectra at the Co K edge were collected during the OER for the pristine and cycled samples (see the experimental set-up scheme and details in Fig. 4a and Supplementary Fig. 20). Operando XANES measurements for fresh LiCoO_{2-x}Cl_x (x = 0, 0.1 or 0.2) showed that the Co K edge shifted to higher energy regions during the anodic polarization (Fig. 4b and Supplementary Fig. 21a,c). Positive shifts suggest

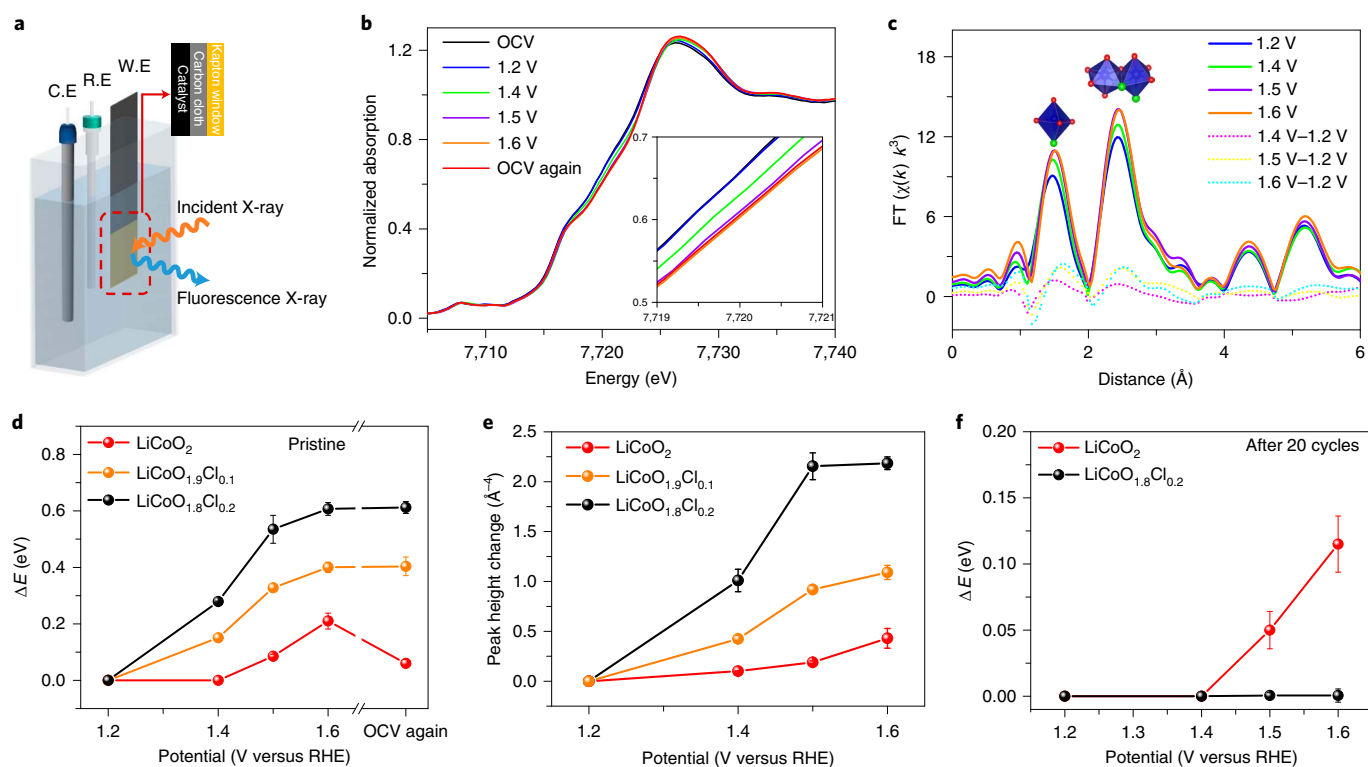


Fig. 4 | Operando XAFS test. **a**, Experimental set-up scheme. C.E., counter electrode; R.E., reference electrode; W.E., working electrode. **b, c**, Co K-edge XANES spectra recorded at different potentials for fresh $\text{LiCoO}_{1.8}\text{Cl}_{0.2}$ (**b**) and corresponding Fourier-transformed k^3 -weighted EXAFS (**c**). **d, e**, Co K-edge shift (**d**) and Co–Co coordination peak amplitude change (**e**) at varied electrochemical potentials for fresh samples. **f**, Co K-edge shift for cycled samples (20 times). Error bars in **d–f** represent standard deviations of data from two measurements.

an increase in the Co valence state. At the initial OER polarization, $\text{LiCoO}_{1.8}\text{Cl}_{0.2}$ manifested the largest positive edge shift, that is, 0.6 eV at 1.6 V versus RHE, followed by $\text{LiCoO}_{1.9}\text{Cl}_{0.1}$ (0.4 eV) and pristine LiCoO_2 (0.2 eV), as shown in Fig. 4d. Moreover, the Co redox transition of $\text{LiCoO}_{1.8}\text{Cl}_{0.2}$ was found to be confined within the +2/+3 region: the Co K edge of the OER-polarized $\text{LiCoO}_{1.8}\text{Cl}_{0.2}$ was still below that of pristine LiCoO_2 with Co^{3+} (Supplementary Fig. 22), which suggests $\text{LiCoO}_{1.8}\text{Cl}_{0.2}$ retained mixed $\text{Co}^{2+}/\text{Co}^{3+}$ states on average during and after the OER. For LiCoO_2 , the positive shift of the Co K edge was attributed to the oxidation of Co^{3+} to Co^{4+} . Cl doping was demonstrated to modify the in situ Co redox transitions of LiCoO_2 during the OER, which is also supported by the cyclic voltammetry scans (Supplementary Fig. 23). The oxidation of $\text{LiCoO}_{1.8}\text{Cl}_{0.2}$ started before 1.4 V versus RHE (Fig. 4d), in sharp contrast to LiCoO_2 , which corroborated that the $\text{Co}^{2+}/\text{Co}^{3+}$ transition in $\text{LiCoO}_{1.8}\text{Cl}_{0.2}$ initiated at a lower potential than the $\text{Co}^{3+}/\text{Co}^{4+}$ transition in LiCoO_2 (ref. 27). This resulted in a greater increase in the cobalt valence in $\text{LiCoO}_{1.8}\text{Cl}_{0.2}$ than that in LiCoO_2 within the same anodic potential range. When the OER polarization ceased, the Co K edge of $\text{LiCoO}_{1.8}\text{Cl}_{0.2}$ did not revert to the lower-energy position (Fig. 4d), which suggests the stability of oxidized Co in Cl-doped LiCoO_2 . In contrast, tetravalent Co in oxidized LiCoO_2 was subject to reduction to a lower stable valence state⁴¹.

The partial oxidation of the tested samples can also be inferred by the operando EXAFS (Fig. 4c and Supplementary Fig. 21b,d). The fitting of the Fourier-transformed EXAFS (Supplementary Figs. 24 and 25) demonstrated an increased Co–O coordination number during the anodic polarization, that is, 4.55 to 5.02 for $\text{LiCoO}_{1.8}\text{Cl}_{0.2}$ and 5.88 to 5.96 for LiCoO_2 (Supplementary Tables 9 and 10). The larger Co–O coordination number increase of $\text{LiCoO}_{1.8}\text{Cl}_{0.2}$ concurred with its greater degree of Co valence-state change^{11,36}. Moreover, a growth

of the Co–Co coordination peak with a fitted Co–Co distance of ~ 2.8 Å was observed (dashed lines in Fig. 4c and Supplementary Fig. 21b,d). Figure 4e shows that $\text{LiCoO}_{1.8}\text{Cl}_{0.2}$ features the largest growth of the Co–Co coordination peak, followed by $\text{LiCoO}_{1.9}\text{Cl}_{0.1}$ and LiCoO_2 . Previous studies attributed this notable increase of edge-sharing octahedra motifs to the formation of layered (oxy) hydroxides^{11,36}. However, it is challenging to confirm this by only EXAFS because $\text{LiCoO}_{2-x}\text{Cl}_x$ shares a similar layered structure to that of cobalt (oxy)hydroxide, as well as the edge-sharing octahedra motif with an almost identical Co–Co distance (~ 2.8 Å). This aspect was validated by post-mortem characterizations and is discussed below.

The XANES and EXAFS of $\text{LiCoO}_{1.8}\text{Cl}_{0.2}$ do not noticeably change after 20 cyclic voltammetry cycles (Supplementary Figs. 26a,b), which suggests that the restructuring process was completed irreversibly. On the contrary, cycled LiCoO_2 persistently shifted the Co K edge (Fig. 4f and Supplementary Fig. 26c) and increased the coordination peak intensities (Supplementary Fig. 26d), which indicates either the restructured phase was unstable or the restructuring process had not completed.

Distinct restructured surface. The high-resolution transmission electron microscopy (TEM) images in Fig. 5a and Supplementary Fig. 27 show an amorphous layer on the surface of cycled $\text{LiCoO}_{1.8}\text{Cl}_{0.2}$, in contrast to the case of cycled LiCoO_2 . Given the ordered atomic distribution on the surface of pristine $\text{LiCoO}_{1.8}\text{Cl}_{0.2}$, surface restructuring was facilitated in situ during the OER. The STEM-EDS (Fig. 5b) further demonstrated that the restructured surface contained Co, O and Cl, and the line profile scans indicated no clear loss of Cl in the surface domain. The surface Cl to Co atomic ratio determined by XPS (Supplementary Fig. 28) remained similar for pristine and cycled $\text{LiCoO}_{1.8}\text{Cl}_{0.2}$.

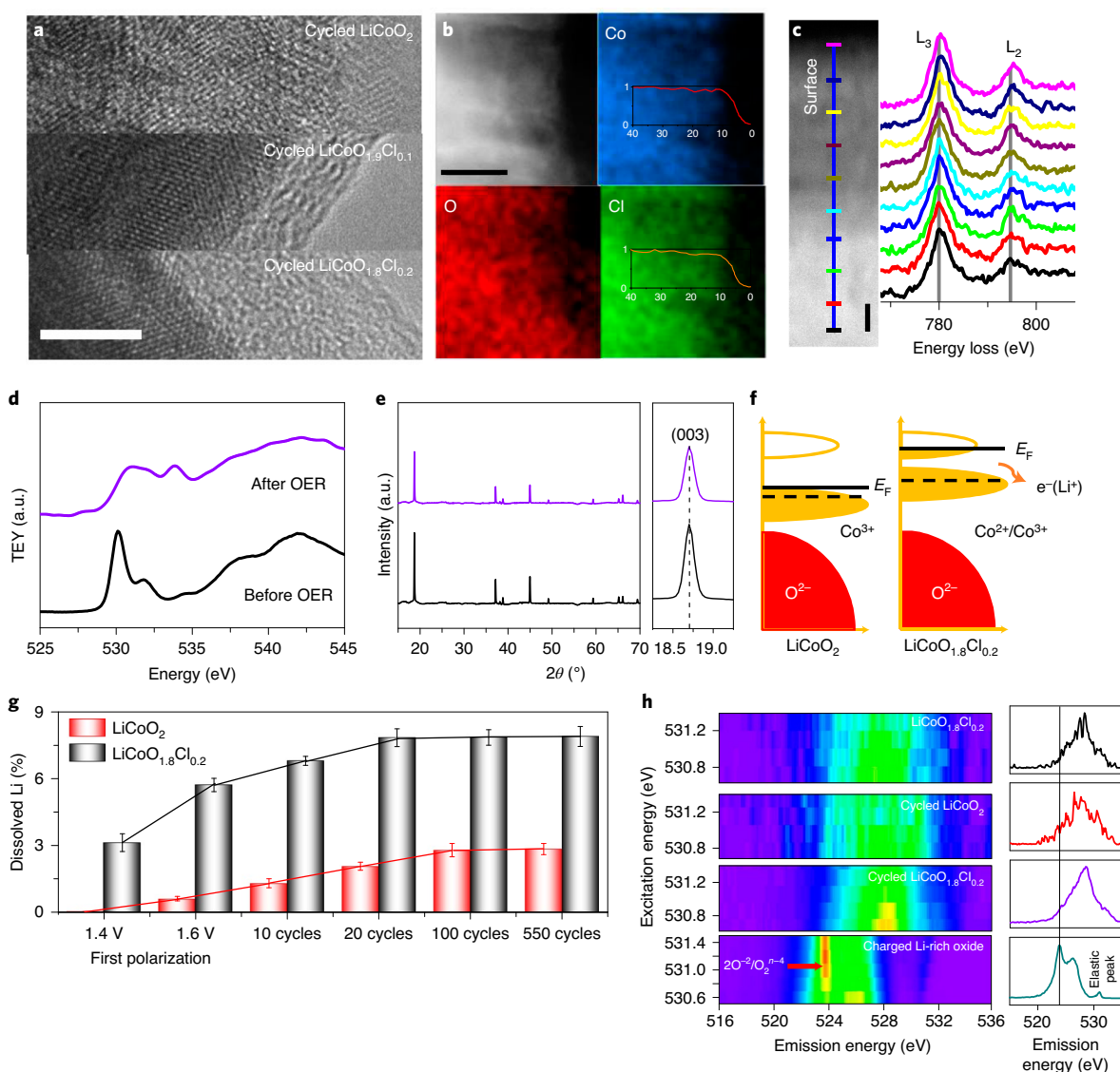


Fig. 5 | Postmortem characterization of cycled $\text{LiCoO}_{1.8}\text{Cl}_{0.2}$. **a**, TEM images. Scale bar, 5 nm. **b**, HAADF-STEM image and corresponding EDS mapping of the surface region. Scale bar, 20 nm. Inset: EDS line cut. **c**, Individual Co L-edge EELS along the beam path indicated by the blue line in the HAADF-STEM image. **d**, O K-edge TEY sXAS of $\text{LiCoO}_{1.8}\text{Cl}_{0.2}$. **e**, Synchrotron XRD of pristine (bottom) and cycled (top) $\text{LiCoO}_{1.8}\text{Cl}_{0.2}$ (1,000 times). **f**, Scheme of the electronic band evolution before (solid line) and after (dashed line) electrochemical OER. **g**, Leached Li amount determined by ICP-MS after varying cycles. Error bars represent standard deviations of two measured data. **h**, O K-edge RIXS maps of pristine $\text{LiCoO}_{1.8}\text{Cl}_{0.2}$, cycled $\text{LiCoO}_{1.8}\text{Cl}_{0.2}$ (100 times), cycled LiCoO_2 (100 times) and charged $\text{Li}[\text{Li}_{0.144}\text{Ni}_{0.136}\text{Mn}_{0.544}\text{Co}_{0.136}]\text{O}_2$ to 4.75 V versus Li/Li^+ at 10 mA g^{-1} , with the line-cut spectra of the RIXS map at an excitation energy of 531 eV shown on the right.

The BF-STEM image (Supplementary Fig. 29) shows short remnant lattice fringes in the reconstructed surface domain. The FFT-derived lattice spacing ($\sim 0.26 \text{ nm}$) can be indexed to cobalt (oxy)hydroxide, which is distinctive from that of the $\text{LiCoO}_{1.8}\text{Cl}_{0.2}$ or spinel $\text{Li}_{1\pm x}\text{Co}_2\text{O}_4$ (ref. 21). The presence of hydroxyl groups on the surface of cycled $\text{LiCoO}_{1.8}\text{Cl}_{0.2}$ was supported by the O K-edge sXAS (Fig. 5d): the energy resonance at $\sim 530 \text{ eV}$ was assigned to the hybridization between O and Co, and the rise of the resonance near $\sim 535 \text{ eV}$ after the OER demonstrated the increased presence of hydroxy groups^{13,42}. O 1s XPS fittings (Supplementary Fig. 30) demonstrate a higher proportion of hydroxyl groups on the surface of cycled $\text{LiCoO}_{1.8}\text{Cl}_{0.2}$ than on that of cycled LiCoO_2 .

Electron energy loss spectroscopy (EELS) was applied to investigate the electronic configuration of the reconstructed surface. There was no detectable shift of the O K-edge and Co

L-edge EELS spectra within the reconstructed surface of cycled $\text{LiCoO}_{1.8}\text{Cl}_{0.2}$ (Supplementary Fig. 31), which suggests a uniform electronic environment. In contrast, we detected a shift to higher energy for Co L-edge EELS in the surface domain compared with that of the bulk (Fig. 5c), demonstrating that the surface Co of $\text{LiCoO}_{1.8}\text{Cl}_{0.2}$ was oxidized. This trend is consistent with the surface-sensitive sXAS results (Supplementary Fig. 32). The $\text{Co}^{3+}/\text{Co}^{4+}$ transition usually takes place at around 1.5 V versus RHE¹⁴, which agrees well with the operando XANES results that to oxidize Co^{3+} in LiCoO_2 required potentials larger than 1.4 V versus RHE (Fig. 4d). $\text{LiCoO}_{1.8}\text{Cl}_{0.2}$ completed most of the cobalt valence increase by 1.5 V versus RHE (Fig. 4d), which avoided the further oxidation into Co^{4+} . Synchrotron XRD (Fig. 5e) confirmed the well-maintained bulk structure of $\text{LiCoO}_{1.8}\text{Cl}_{0.2}$ after the OER. Moreover, the XRD patterns for the (003) plane retained the same

2θ angle, which indicates that there was no notable loss of Li or oxidation of Co in the crystalline bulk⁴³.

A series of inductively coupled plasma mass spectrometry (ICP-MS) analyses were conducted after various cycles to track the proportion of lithium extracted from the loaded electrode particles (Fig. 5g). Leached Co was not detected in the cycled samples. Combining the above findings of a well-maintained Cl, the presence of hydroxyl groups and loss of surface Li, the composition of the restructured surface for cycled $\text{LiCoO}_{1.8}\text{Cl}_{0.2}$ was determined to be Cl-containing Co (oxy)hydroxide. The DFT calculation (Supplementary Fig. 33) further supported that Cl resided at the intralayer of the structure. $\text{LiCoO}_{1.8}\text{Cl}_{0.2}$ allowed more lithium extraction but quenched this process faster than that in the case of LiCoO_2 (Fig. 5g). Facile lithium extraction of $\text{LiCoO}_{1.8}\text{Cl}_{0.2}$ was initiated at lower positive potentials (1.4 V versus RHE) during the first cycle and completed within 20 cycles, in agreement with the Co oxidation from the operando XANES. In contrast, LiCoO_2 underwent delithiation persistently for 100 cycles and took a longer time for the restructuring process to complete. Lithium diffusion is fast in two-dimensional lithium layers of $\text{LiCoO}_{2-x}\text{Cl}_x$, and the expanded Li layers of $\text{LiCoO}_{1.8}\text{Cl}_{0.2}$ can potentially further favour the lithium mobility^{26,33}. However, increasing the disorder degree in the lattice will disrupt the Li migration pathway and substantially lower the Li diffusivity⁴⁴. The restructured amorphous surface, triggered by the facile delithiation of $\text{LiCoO}_{1.8}\text{Cl}_{0.2}$, behaved as a lithium blocking layer (which prohibited further Li extraction and Co oxidation) and terminated the surface reconstruction. Surprisingly, this restructured surface was found to be stable for 1,000 cycles (Supplementary Fig. 34), which supports the long OER stability. Delithiation during the OER was also reported for other Li-containing TMOs^{45,46}. However, neither engineering the delithiation potential nor controlling the Li leaching level were accessible in previous work. Further manipulating the dynamic surface restructuring via rationally modulating the in situ delithiation, as this work did, was seldom reported.

Recent studies proposed that the surface reconstruction could be associated with the anionic redox of lattice oxygen during the OER^{21,22}. However, to detect the oxidized oxygen states and distinguish them from the strong signals from Co–O hybridization is challenging through conventional O K-edge sXAS⁴⁷. Thus, we studied the oxygen states before and after the OER via resonant inelastic X-ray scattering (RIXS), which is established as the tool-of-choice for detecting the oxygen oxidized to a non-divalent state^{47,48}. In comparison, we show the O K-edge RIXS maps of a charged Li-rich electrode in Fig. 5h, which displays the characteristic feature of the oxidized oxygen at ~ 531 and ~ 524 eV of the excitation and emission energies, respectively⁴⁷, which correspond to the oxidation of O^{2-} . Such a feature was also reported in deeply delithiated LiCoO_2 , in which oxidized oxygen was triggered⁴⁸. In contrast, such a RIXS feature was not detected in pristine $\text{LiCoO}_{1.8}\text{Cl}_{0.2}$, cycled $\text{LiCoO}_{1.8}\text{Cl}_{0.2}$ or cycled LiCoO_2 , as shown in the RIXS images and clearly presented in the RIXS cuts with a 531 eV excitation energy, which suggests no obvious formation of oxidized oxygen for the restructured $\text{LiCoO}_{2-x}\text{Cl}_x$. From our DFT calculations, the O 2p band centre of $\text{LiCoO}_{1.8}\text{Cl}_{0.2}$ was downshifted away from the Fermi level by ~ 0.8 eV relative to that of LiCoO_2 (schemed in Fig. 5f). $\text{LiCoO}_{1.8}\text{Cl}_{0.2}$ retained a mixed $\text{Co}^{2+}/\text{Co}^{3+}$ state after the OER, potentially keeping the O 2p band away from the Fermi level and generating no oxygen ligand holes⁴⁹.

Roles of Cl. Based on the above, Cl-doped cobalt (oxy)hydroxide was generated on the surface of cycled $\text{LiCoO}_{1.8}\text{Cl}_{0.2}$. On the contrary, the surface of cycled LiCoO_2 was reconstructed into spinel-type $\text{Li}_{1-x}\text{Co}_2\text{O}_4$ ($0 < x < 1$) (refs. ^{28,33}), as supported by the spherical aberration-corrected TEM (Cs-TEM), FFT, XPS, XRD and EXAFS results (Supplementary Note 4 and Supplementary

Fig. 35). The Co L-edge sXAS and fitting (Supplementary Fig. 36) further confirmed that the restructured surface of cycled LiCoO_2 contained Co^{4+} . In addition, cycling pre-delithiated $\text{Li}_{1-x}\text{CoO}_2$ with the same protocol could only generate a spinel-type restructured surface (Supplementary Note 5 and Supplementary Fig. 37). The electrolyte soaking in KOH solutions was also precluded as an influence on the surface restructuring of layered $\text{LiCoO}_{2-x}\text{Cl}_x$ (Supplementary Fig. 38). It is clear that Cl doping redirects the in situ surface reconstruction of LiCoO_2 from the same layered structure, illustrated schematically in Fig. 6a. Such a change was ascribed to the modified Co redox transitions, which initiated the in situ Co oxidation and Li extraction of $\text{LiCoO}_{1.8}\text{Cl}_{0.2}$ at a lower positive potential (less than 1.4 V versus RHE), whereas Cl-free LiCoO_2 required a potential higher than 1.4 V versus RHE to oxidize LiCoO_2 and extract Li (Fig. 4d and Fig. 5g). Thus, Cl doping contributed to a larger increase in the Co valence and a greater degree of Li extraction. Moreover, via avoiding the transformation into metastable Co^{4+} cations, stabilization of the restructuring process was accelerated, as shown in Fig. 4f and Fig. 5g.

By using DFT energetics, we further investigated how Cl doping could alter the structural phase transformation path from the spinel-type $\text{Li}_{1-x}\text{Co}_2\text{O}_4$ formation into oxyhydroxide formation. To induce a structural phase transformation of layered LiCoO_2 in a certain domain of the particle surface, delithiation in the structural domain is considered to be a prerequisite^{22,28}. We thus conceived three different reaction paths: (1) LiCo_2O_4 -type spinel structure formation via partial delithiation, (2) Co_3O_4 -type spinel structure formation accompanied by an oxygen gas evolution via full delithiation and (3) oxyhydroxide structure formation via full delithiation. DFT energetics for the three different paths were obtained under the polarization potential of 1.6 V versus RHE, as shown in Fig. 6c,d. Although the DFT energetics were calculated by removing a half or full lithium in the simulation cell, note that the simulation cell represents only the small structural domain in the particle surface, and thus the delithiation degree of the entire particle could be much smaller.

For Cl-free LiCoO_2 , the delithiation is energetically unfavourable, as shown in Fig. 6c, and thus the formation of Co_3O_4 -type spinel (path 2) or oxyhydroxide (path 3) via a full delithiation is kinetically unfavourable. Moreover, partially delithiated $\text{Li}_{1-x}\text{CoO}_2$ can facilitate the phase transformation into a spinel-like structure (path 1, marked as a red dotted line in Fig. 6c), consistent with previous calculations^{31,32}. Indeed, we experimentally found the formation of lithium-containing $\text{Li}_{1-x}\text{Co}_2\text{O}_4$ -type spinel structure on the restructured surface of layered LiCoO_2 (Supplementary Fig. 35)^{33,50}. When Cl is included in LiCoO_2 , the delithiation becomes energetically favourable by substantially lowering the delithiation potential. As shown in Fig. 6d, unlike the Cl-free LiCoO_2 case, all the reaction paths become mostly downhill, and thus are conceived to be thermodynamically controlled. Consequently, the (oxy)hydroxide structure, which is the most energetically stable, was formed on the surface of cycled Cl-containing $\text{LiCoO}_{1.8}\text{Cl}_{0.2}$ (path 3, marked as a blue dotted line in Fig. 6d). Further, the calculated surface formation energies that considered the solvation effect also supported that the Cl-doping yields a favourable formation of oxyhydroxide structure at the surface (Supplementary Note 6 and Supplementary Table 11).

Transition metal (oxy)hydroxides are generally more OER-active than their spinel counterparts^{21,22}. The calculated OER free-energy diagram further demonstrated that Cl doping with varying concentrations lowered the OER overpotential of cobalt (oxy)hydroxide surfaces. The emboldened potential limiting steps indicate that 10 and 15% Cl doping decreased the overpotential by 360 and 610 mV, respectively (Fig. 6b, Supplementary Figures 39 and 40, and Supplementary Note 7). Moreover, Cl doping shortens the bandgap of LiCoO_2 (Fig. 2b), which provides a more conductive scaffold to

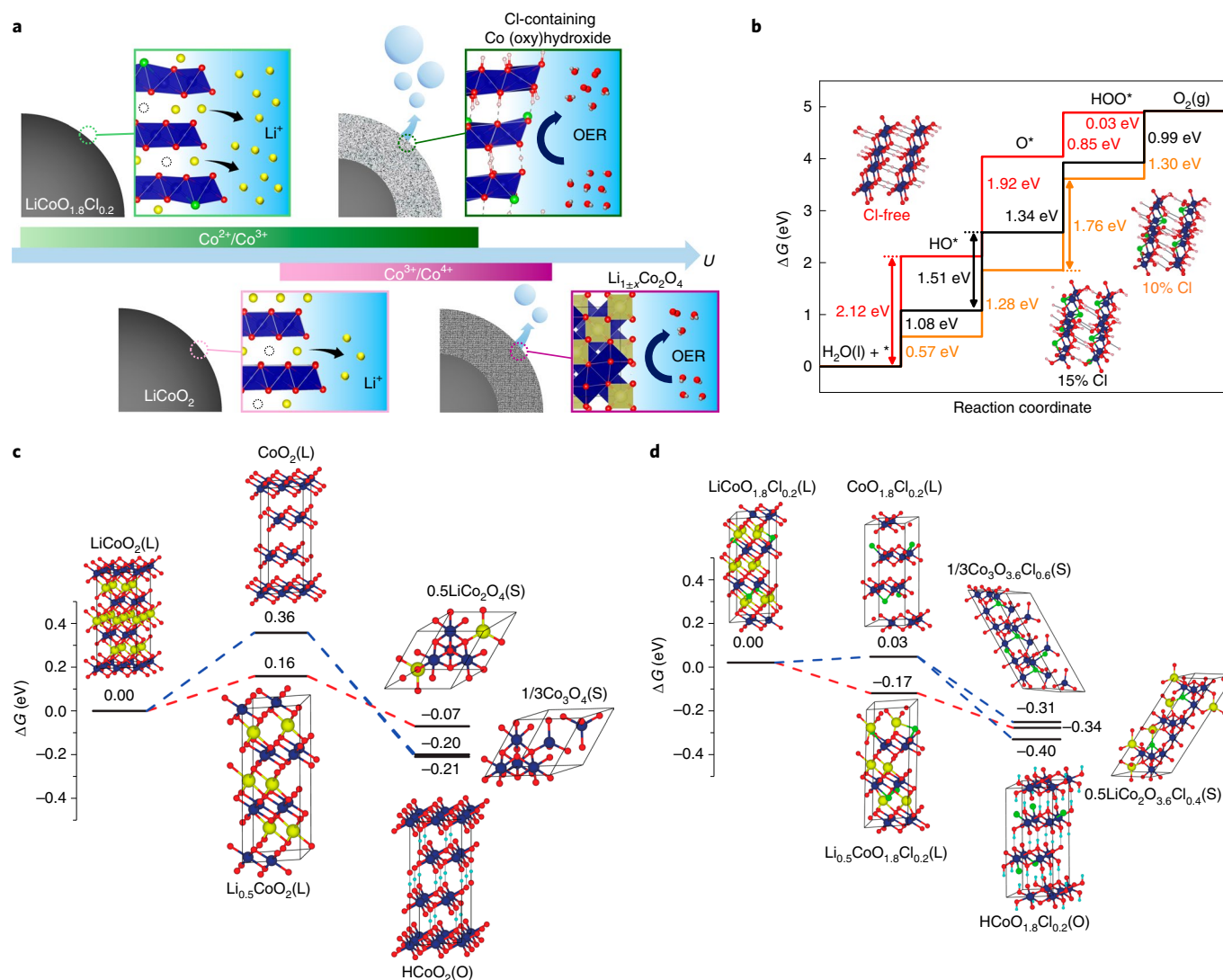


Fig. 6 | Theoretical understanding of Cl doping in redirecting surface restructuring. **a**, Schematic illustration of the in situ surface restructuring process of LiCoO_2 and $\text{LiCoO}_{1.8}\text{Cl}_{0.2}$ during the OER. **b**, Calculated OER free-energy diagrams at $U=0\text{ V}$ for Cl-free (red), 10% Cl-doped (yellow) and 15% Cl-doped (black) O-terminated (01 $\bar{1}2$) surfaces of cobalt (oxy)hydroxide. **c,d**, DFT-calculated reaction energy profile at 1.6 V versus RHE: the relative energies of spinel-type structures (S) and (oxy)hydroxides (O) from layered structures (L) with respect to the energy of layered LiCoO_2 (**c**) and $\text{LiCoO}_{1.8}\text{Cl}_{0.2}$ (**d**).

support the restructured (oxy)hydroxide surface and contribute to faster charge transfer kinetics. All of the above lead to the efficient OER activity of $\text{LiCoO}_{1.8}\text{Cl}_{0.2}$.

Discussion

With layered LiCoO_2 , this work provided a redox-tuning method to modulate the dynamic surface restructuring via precisely manipulating the in situ catalyst leaching. It engineered the cation leaching potential, modulated the in situ leaching level and redirected the dynamic surface restructuring pathway, which advanced the control of the in situ formed catalytically active surface. Owing to the challenge of controlling in situ catalyst leaching, reported surface restructuring was usually activated in some way or left unactivated, and the catalyst surface tended to be pristine or a specific restructured one^{11,21,40}. In marked contrast, by modulating the amount of in situ leached cations, the restructured surface in this work was precisely tuned with many more possibilities. Specifically, the Co valence state, Li composition and lattice phase of the restructured surface were facily modulated by adjusting the transition metal redox/cation leaching level. We further demonstrated the bypass

of the less-active reconstructed surface (that is, spinel oxide) and guided the formation of the more-active amorphous (oxy)hydroxide starting from the same parent structure. In addition, our methodology paved an avenue to favourable in situ reconstruction properties: beneficial leaching initiated at a lower operating potential and the more favourable surface restructuring completed during a shorter cycling time, catalytic activity was enhanced and the self-terminated surface phase rendered an extended life-time. It is also worth mentioning that the modulated surface restructuring process via tuning the cationic redox did not involve the obvious activation of anionic oxygen redox, which avoided the loss of lattice oxygen¹⁸ or transition metal cations¹¹ as potential active centres.

The reported method could be potentially generalized to a large family of redox-active materials that compensate the transition metal redox with the intercalation/deintercalation of cations, for example, layered oxides (AMO_2 ; A = alkaline metal, M = transition metal) and spinel-type oxides (AM_2O_4 ; A = alkaline metal, M = transition metal). In addition to basic solutions, the redox-tuning method has the potential to be applied to neutral and acidic electrolytes to modulate the in situ leaching and the surface restructuring of OER

electrocatalysts. Shao-Horn and co-workers found that the electrolyte pH substantially influenced the surface nature of LiCoO_2 and LiCoPO_4 that undergo the OER⁵⁰. Different electrolytes substantially modify the surface chemistry of catalysts and influence their leaching levels, so tuning the cationic redox is expected to play an important role. The present study could also serve as a reference to other categories of pre-catalysts (for example, transition metal nitrides, phosphides and/or chalcogenides), and inspire to control their in situ leaching and modulate the dynamic surface restructuring during water electrolysis. In short, this work represents a step forward in manipulating the in situ formed catalytically active species and in designing high-performance OER electrocatalysts.

Methods

Sample preparation. The layered LiCoO_2 was prepared via a solid-state route according to the previous literature²⁷. A stoichiometric amount of raw reactants, which included $\text{LiOH}\cdot\text{H}_2\text{O}$ (>99%, Sigma Aldrich) and Co_2O_3 (>99%, Shanghai Zhanyun Chemical Co., Ltd), were mixed well and then sintered at 850 °C for 12 h in ambient air, with a heating and cooling ramping rate of 10 °C min^{-1} . Cl-doped LiCoO_2 was obtained following the same strategy but replacing parts of Co_2O_3 with $\text{CoCl}_2\cdot 6\text{H}_2\text{O}$ (>98%, Alfa Aesar).

BSCF5582 was synthesized by a sol-gel method. The stoichiometric amounts of $\text{Ba}(\text{NO}_3)_2$ (>99%, Sigma Aldrich), $\text{Sr}(\text{NO}_3)_2$ (>99%, Sigma Aldrich), $\text{Co}(\text{NO}_3)_2\cdot 6\text{H}_2\text{O}$ (>98%, Alfa Aesar) and $\text{Fe}(\text{NO}_3)_3\cdot 9\text{H}_2\text{O}$ (>98%, Sigma Aldrich) were dissolved into deionized water, followed by the addition of EDTA (>98.5%, Sigma Aldrich) and citric acid (>99%, Alfa Aesar) with the molar ratio of total metal ion:EDTA: citric acid equal to 1:1:2. The pH of the solution was adjusted to ~6 by adding ammonium hydroxide. Subsequently, the transparent gel, obtained by stirring and evaporating the solution at 90 °C, was heated in an oven at 250 °C for 5 h. Finally, the formed black solid precursor was fired inside a box furnace in the air at 1,000 °C for 10 h to yield BSCF5582. RuO_2 (99.9%, Sigma Aldrich) and Co_3O_4 (>99%, Alfa Aesar) were used without further treatment.

Characterizations. XRD was measured at room temperature with synchrotron radiation at the BL9B beamline with a Si(111) crystal monochromator in the Pohang Accelerator Laboratory (PAL). The corresponding Rietveld refinement was conducted with the FullProf program. The ex situ sXAS was collected in the TEY mode at the BL10D beamline in the PAL. The TEY was detected by probing the drain current from the sample with a picoammeter (Keithley 6485). The chamber pressure was held at 5×10^{-9} torr. The ex situ XANES and EXAFS measurements were performed in transmission mode at the BL7D beamline in the PAL. The ion chamber used for the XAFS test has a length of 30 cm with a pressure of 1 atm (filled with pure N_2 gas) and a voltage of 3 kV. The operando XAFS tests were conducted in the fluorescence mode at the BL10C beamline in the PAL. The ATHENA program was used to process the acquired EXAFS data, which were then analysed in the ARTEMIS program integrated with the IFFFIT software package⁵¹. The RIXS spectra were collected at Beamline 8.0.1 at the Advanced Light Source, Lawrence Berkeley National Laboratory.

TEM images were taken by Tecnai F20 (FEI). The atomic structure and chemical composition were examined using a spherical aberration-corrected JEM ARM-200F microscope (Cold FEG Type, JEOL) equipped with an energy dispersive X-ray spectroscopy detector of the silicon drift detector type (solid angle 0.9 sr X-MaxN 100TLE, Oxford Instruments) and EELS detector (965 GIF Quantum ER, Gatan) at 200 kV installed at the National Center for Interuniversity Research Facilities (NCIRF) of Seoul National University. The information limit of the HRTEM and the HAADF-STEM after the Cs-correction was 0.07 and 0.08 nm, respectively. The HAADF-STEM images were acquired with a camera length of 8 cm and a collection angle of 68–280 mrad. For the STEM-EELS measurements, the energy dispersion was set at 0.25 eV per channel. The full-width at half-maximum of the zero-loss peak in vacuum was 1.3 eV. The convergence and collection semi-angles were 19.0 and 39.6 mrad, respectively. For the STEM-EDS analyses, the chemical maps were acquired with a probe size of 0.13 nm and a probe current of 40 pA.

The morphology was checked by scanning electron microscopy (JEOL, 6300). The EDS was scanned with a field-emission scanning electron microscope (Melin Compact). XPS (PHI5600) was collected inside a vacuum chamber (10^{-8} – 10^{-9} Pa) using a monochromatic Al-source X-ray. The Brunauer–Emmett–Teller surface area was obtained by measuring N_2 adsorption and desorption isotherms at 77 K with an analyser (Beckman Coulter, SA3100 model). The corresponding pore-size distribution was calculated by following the Barrett–Joyner–Halenda formula. The elemental contents were analysed by ICP-MS (NexION 350D Perkin-Elmer) with a mass resolution of 0.3–3.0 a.m.u.

Electrochemical assessment. The OER performance was evaluated in 1 M KOH with a three electrode set-up via a rotating ring-disk electrode (RRDE-3A, BAS Inc.) device. The catalyst-modified GC (4 mm in diameter), coiled Pt wire

and Ag/AgCl (ALS) served as the working, counter and reference electrode, respectively. The polarization potential on the working electrode was controlled by an ALS2325E potentiostat, and was corrected by compensating the ohmic drop of the electrolyte, with its resistance determined by electrochemical impedance spectroscopy. The catalyst ink was prepared by dispersing the mixture of 5 mg of active material with 5 mg of Vulcan XC-72 carbon into a solution made of 1.9 ml of ethanol and 0.1 ml of 5 wt% Nafion. Next, the obtained suspension was sonicated in an ice water bath for 1 h. The GC electrode was polished with alumina slurry (BAS Inc.) and then sonicated in an ethanol and water mixture to achieve the mirror surface. Finally, 10 μl of the homogeneously dispersed sample was drop casted onto the freshly polished GC disk using a micropipette and left to dry naturally in the air. A chronopotentiometry test was conducted with the examined catalyst loaded on carbon paper (8 mm \times 8 mm in size) with a mass loading of $\sim 0.4 \text{ mg}_{\text{oxide}} \text{ cm}_{\text{geo}}^{-2}$.

Computational methods. All the spin-polarized first-principle calculations were performed using the Vienna ab initio simulation package^{52,53} with a plane-wave basis set and a projector-augmented wave pseudopotentials⁵⁴. We set the kinetic energy cutoff as 500 eV, and described the exchange correlation using the Perdew–Burke–Ernzerhof functional⁵⁵ under the generalized gradient approximation (GGA) scheme. The strongly localized 3d orbital of Co was simulated using the GGA+U method with U_{eff} value to be 4.91 eV (ref. 56). LiCoO_2 in the space group $R\bar{3}m$ was chosen and a supercell of $2 \times 2 \times 1$ was employed for all the calculations in which the total atom numbers of Li, Co and O were 12, 12 and 24, respectively. For Cl substitution, one or two of the O atoms were replaced with Cl to simulate $\text{LiCoO}_{1.9}\text{Cl}_{0.1}$ ($\text{Li}_{12}\text{Co}_{12}\text{O}_{22}\text{Cl}$) and $\text{LiCoO}_{1.8}\text{Cl}_{0.2}$ ($\text{Li}_{12}\text{Co}_{12}\text{O}_{22}\text{Cl}_2$). The Brillouin zone was sampled by Γ -centred k points of $5 \times 5 \times 2$ for relaxation and of $10 \times 10 \times 4$ for the density of states and Bader charge analysis⁵⁷. Hydrogen gas and oxygen gas were calculated in a $20 \text{ \AA} \times 20 \text{ \AA} \times 20 \text{ \AA}$ cell box to prevent cell-to-cell interaction with single Γ -point sampling, and body-centred cubic (BCC) Li were sampled with Γ -centred k points of $20 \times 20 \times 20$. Using the computational hydrogen electrode model, the chemical potentials of H^+ and e^- were determined as $\mu[\text{H}^+] + \mu[\text{e}^-] = 1/2 G_{\text{H}_2(\text{g})} - eU_{\text{RHE}}$. Similarly, the chemical potentials of Li^+ and e^- were determined as $\mu[\text{Li}^+] + \mu[\text{e}^-] = G_{\text{Li}(\text{BCC})} - eU_{\text{Li}/\text{Li}^+} = E_{\text{Li}(\text{BCC})} - e(U_{\text{RHE}} + 3.04 \text{ V} - 0.0591 \text{ pH})$, which yields $\mu[\text{H}^+] - \mu[\text{Li}^+] = 1/2 G_{\text{H}_2(\text{g})} - E_{\text{Li}(\text{BCC})} + e(3.04 \text{ V} - 0.0591 \text{ pH})$.

To assess the surface effect on the phase restructuring energetics, we calculated the surface formation energy, ΔE_{surf} , for the stable low-index surfaces—the (0001) surface of Co oxyhydroxide⁵⁸ and the (111) surface of spinel structures⁵⁹, which are considered to predominantly exist at the surface⁶⁰.

To compute the OER activity, we modelled the catalyst surface using the O-terminated (01 $\bar{1}$ 2) surface of Co oxyhydroxide, which is known to be the preferred termination of CoOOH (ref. 61). DFT-optimized structures of the Co oxyhydroxide surface with and without Cl are shown in the inset of Fig. 6b. The reciprocal space was sampled using the $3 \times 3 \times 1$ Monkhorst–Pack grid⁶². We considered the solvation effect using the VASPsol method⁶³. The atomic coordinates of the optimized models are provided in Supplementary Data 1.

Data availability

Most data supporting the findings of this study are available from the main text of the article and its Supplementary Information. More data can be obtained from the corresponding authors upon reasonable request.

Received: 11 July 2020; Accepted: 8 January 2021;

Published online: 1 March 2021

References

- Körner, A., Tam, C., Bennett, S. & Gagné, J. *Technology Roadmap—Hydrogen and Fuel Cells* (International Energy Agency, 2015).
- Jin, S. Are metal chalcogenides, nitrides, and phosphides oxygen evolution catalysts or bifunctional catalysts? *ACS Energy Lett.* **2**, 1937–1938 (2017).
- Suen, N.-T. et al. Electrocatalysis for the oxygen evolution reaction: recent development and future perspectives. *Chem. Soc. Rev.* **46**, 337–365 (2017).
- Song, F. et al. Transition metal oxides as electrocatalysts for the oxygen evolution reaction in alkaline solutions: an application-inspired renaissance. *J. Am. Chem. Soc.* **140**, 7748–7759 (2018).
- Li, T. et al. Atomic-scale insights into surface species of electrocatalysts in three dimensions. *Nat. Catal.* **1**, 300–305 (2018).
- Friebel, D. et al. Identification of highly active Fe sites in (Ni,Fe)OOH for electrocatalytic water splitting. *J. Am. Chem. Soc.* **137**, 1305–1313 (2015).
- Subbaraman, R. et al. Trends in activity for water electrolyser reactions on 3d M(Ni,Co,Fe,Mn) hydr(oxy)oxide catalysts. *Nat. Mater.* **11**, 550–557 (2012).
- Man, I. C. et al. Universality in oxygen evolution electrocatalysis on oxide surfaces. *ChemCatChem* **3**, 1159–1165 (2011).
- Suntivich, J., May, K. J., Gasteiger, H. A., Goodenough, J. B. & Shao-Horn, Y. A perovskite oxide optimized for oxygen evolution catalysis from molecular orbital principles. *Science* **334**, 1383–1385 (2011).
- Grimaud, A. et al. Double perovskites as a family of highly active catalysts for oxygen evolution in alkaline solution. *Nat. Commun.* **4**, 2439 (2013).

11. Fabbri, E. et al. Dynamic surface self-reconstruction is the key of highly active perovskite nano-electrocatalysts for water splitting. *Nat. Mater.* **16**, 925–931 (2017).
12. Jiang, H., He, Q., Zhang, Y. & Song, L. Structural self-reconstruction of catalysts in electrocatalysis. *Acc. Chem. Res.* **51**, 2968–2977 (2018).
13. Bergmann, A. et al. Unified structural motifs of the catalytically active state of Co(oxyhydr)oxides during the electrochemical oxygen evolution reaction. *Nat. Catal.* **1**, 711–719 (2018).
14. Jiang, H. et al. Tracking structural self-reconstruction and identifying true active sites toward cobalt oxychloride precatalyst of oxygen evolution reaction. *Adv. Mater.* **31**, 1805127 (2019).
15. Bergmann, A. et al. Reversible amorphization and the catalytically active state of crystalline Co₃O₄ during oxygen evolution. *Nat. Commun.* **6**, 8625 (2015).
16. Seitz, L. C. et al. A highly active and stable IrO₂/SrIrO₃ catalyst for the oxygen evolution reaction. *Science* **353**, 1011–1014 (2016).
17. Chung, D. Y. et al. Dynamic stability of active sites in hydr(oxy)oxides for the oxygen evolution reaction. *Nat. Energy* **5**, 222–230 (2020).
18. Grimaud, A. et al. Activating lattice oxygen redox reactions in metal oxides to catalyse oxygen evolution. *Nat. Chem.* **9**, 457–465 (2017).
19. Hua, B. et al. Activating *p*-blocking centers in perovskite for efficient water splitting. *Chem* **4**, 2902–2916 (2018).
20. Wang, J. et al. Water splitting with an enhanced bifunctional double perovskite. *ACS Catal.* **8**, 364–371 (2018).
21. Wu, T. et al. Iron-facilitated dynamic active-site generation on spinel CoAl₂O₄ with self-termination of surface reconstruction for water oxidation. *Nat. Catal.* **2**, 763–772 (2019).
22. Zhang, S. et al. Spontaneous delithiation under operando condition triggers formation of an amorphous active layer in spinel cobalt oxides electrocatalyst toward oxygen evolution. *ACS Catal.* **9**, 7389–7397 (2019).
23. Burke, M. S., Enman, L. J., Batchellor, A. S., Zou, S. & Boettcher, S. W. Oxygen evolution reaction electrocatalysis on transition metal oxides and (oxy)hydroxides: activity trends and design principles. *Chem. Mater.* **27**, 7549–7558 (2015).
24. Burke, M. S., Kast, M. G., Trotochaud, L., Smith, A. M. & Boettcher, S. W. Cobalt–iron (oxy)hydroxide oxygen evolution electrocatalysts: the role of structure and composition on activity, stability, and mechanism. *J. Am. Chem. Soc.* **137**, 3638–3648 (2015).
25. Trotochaud, L., Young, S. L., Ranney, J. K. & Boettcher, S. W. Nickel–iron oxyhydroxide oxygen-evolution electrocatalysts: the role of intentional and incidental iron incorporation. *J. Am. Chem. Soc.* **136**, 6744–6753 (2014).
26. Zheng, X. et al. Electronic structure engineering of LiCoO₂ toward enhanced oxygen electrocatalysis. *Adv. Energy Mater.* **9**, 1803482 (2019).
27. Maiyalagan, T., Jarvis, K. A., Therese, S., Ferreira, P. J. & Manthiram, A. Spinel-type lithium cobalt oxide as a bifunctional electrocatalyst for the oxygen evolution and oxygen reduction reactions. *Nat. Commun.* **5**, 3949 (2014).
28. Gardner, G. P. et al. Structural requirements in lithium cobalt oxides for the catalytic oxidation of water. *Angew. Chem. Int. Ed.* **51**, 1616–1619 (2012).
29. Lu, Z. et al. Electrochemical tuning of layered lithium transition metal oxides for improvement of oxygen evolution reaction. *Nat. Commun.* **5**, 4345 (2014).
30. Lu, Z. et al. Identifying the active surfaces of electrochemically tuned LiCoO₂ for oxygen evolution reaction. *J. Am. Chem. Soc.* **139**, 6270–6276 (2017).
31. Ceder, G. & Van der Ven, A. Phase diagrams of lithium transition metal oxides: investigations from first principles. *Electrochim. Acta* **45**, 131–150 (1999).
32. Meng, Y. S. & Arroyo-de Dompablo, M. E. First principles computational materials design for energy storage materials in lithium ion batteries. *Energy Environ. Sci.* **2**, 589–609 (2009).
33. Gardner, G. et al. Structural basis for differing electrocatalytic water oxidation by the cubic, layered and spinel forms of lithium cobalt oxides. *Energy Environ. Sci.* **9**, 184–192 (2016).
34. Lu, X. et al. New insight into the atomic structure of electrochemically delithiated O₃-Li_(1-x)CoO₂ (0 ≤ x ≤ 0.5) nanoparticles. *Nano Lett.* **12**, 6192–6197 (2012).
35. Li, G., Zhou, S., Wang, P. & Zhao, J. Halogen-doping in LiCoO₂ cathode materials for Li-ion batteries: insights from ab initio calculations. *RSC Adv.* **5**, 107326–107332 (2015).
36. Kim, B.-J. et al. Functional role of Fe-doping in Co-based perovskite oxide catalysts for oxygen evolution reaction. *J. Am. Chem. Soc.* **141**, 5231–5240 (2019).
37. Patridge, C. J., Love, C. T., Swider-Lyons, K. E., Twigg, M. E. & Ramaker, D. E. In-situ X-ray absorption spectroscopy analysis of capacity fade in nanoscale-LiCoO₂. *J. Solid State Chem.* **203**, 134–144 (2013).
38. Nakai, I. et al. X-ray absorption fine structure and neutron diffraction analyses of de-intercalation behavior in the LiCoO₂ and LiNiO₂ systems. *J. Power Sources* **68**, 536–539 (1997).
39. Yoon, W.-S. et al. Oxygen contribution on Li-ion intercalation–deintercalation in LiCoO₂ investigated by O K-edge and Co L-edge X-ray absorption spectroscopy. *J. Phys. Chem. B* **106**, 2526–2532 (2002).
40. Chen, C.-H. et al. Soft X-ray absorption spectroscopy studies on the chemically delithiated commercial LiCoO₂ cathode material. *J. Power Sources* **174**, 938–943 (2007).
41. Ismail, J., Ahmed, M. F. & Vishnu Kamath, P. Cyclic voltammetric studies of pure and doped films of cobalt hydroxide in 1 M KOH. *J. Power Sources* **36**, 507–516 (1991).
42. Shan, X. et al. Bivalence Mn₂O₃ with hydroxylated interphase for high-voltage aqueous sodium-ion storage. *Nat. Commun.* **7**, 13370 (2016).
43. Reimers, J. N. & Dahn, J. Electrochemical and in situ X-ray diffraction studies of lithium intercalation in Li_xCoO₂. *J. Electrochem. Soc.* **139**, 2091–2097 (1992).
44. Garcia, B., Farcy, J., Pereira-Ramos, J. & Baffier, N. Electrochemical properties of low temperature crystallized LiCoO₂. *J. Electrochem. Soc.* **144**, 1179–1184 (1997).
45. Baumung, M., Kollenbach, L., Xi, L. & Risch, M. Undesired bulk oxidation of LiMn₂O₄ increases overpotential of electrocatalytic water oxidation in lithium hydroxide electrolytes. *ChemPhysChem* **20**, 2981–2988 (2019).
46. Zhou, J. et al. Voltage- and time-dependent valence state transition in cobalt oxide catalysts during the oxygen evolution reaction. *Nat. Commun.* **11**, 1984 (2020).
47. Yang, W. & Devereaux, T. P. Anionic and cationic redox and interfaces in batteries: advances from soft X-ray absorption spectroscopy to resonant inelastic scattering. *J. Power Sources* **389**, 188–197 (2018).
48. Zhang, J.-N. et al. Trace doping of multiple elements enables stable battery cycling of LiCoO₂ at 4.6 V. *Nat. Energy* **4**, 594–603 (2019).
49. Grimaud, A., Hong, W. T., Shao-Horn, Y. & Tarascon, J.-M. Anionic redox processes for electrochemical devices. *Nat. Mater.* **15**, 121–126 (2016).
50. Lee, S. W. et al. The nature of lithium battery materials under oxygen evolution reaction conditions. *J. Am. Chem. Soc.* **134**, 16959–16962 (2012).
51. Newville, M. IFEFFIT: interactive XAFS analysis and FEFF fitting. *J. Synchrotron Radiat.* **8**, 322–324 (2001).
52. Kresse, G. & Furthmüller, J. Efficient iterative schemes for ab initio total-energy calculations using a plane-wave basis set. *Phys. Rev. B* **54**, 11169 (1996).
53. Kresse, G. & Furthmüller, J. Efficiency of ab-initio total energy calculations for metals and semiconductors using a plane-wave basis set. *Comput. Mater. Sci.* **6**, 15–50 (1996).
54. Blöchl, P. E. Projector augmented-wave method. *Phys. Rev. B* **50**, 17953 (1994).
55. Perdew, J. P., Burke, K. & Ernzerhof, M. Generalized gradient approximation made simple. *Phys. Rev. Lett.* **77**, 3865 (1996).
56. Zhou, F., Cococcioni, M., Marianetti, C. A., Morgan, D. & Ceder, G. First-principles prediction of redox potentials in transition-metal compounds with LDA + *U*. *Phys. Rev. B* **70**, 23521 (2004).
57. Yu, M. & Trinkle, D. R. Accurate and efficient algorithm for Bader charge integration. *J. Chem. Phys.* **134**, 064111 (2011).
58. Bajdich, M., Garcia-Mota, M., Vojvodic, A., Nørskov, J. K. & Bell, A. T. Theoretical investigation of the activity of cobalt oxides for the electrochemical oxidation of water. *J. Am. Chem. Soc.* **135**, 13521–13530 (2013).
59. Su, D., Dou, S. & Wang, G. Single crystalline Co₃O₄ nanocrystals exposed with different crystal planes for Li–O₂ batteries. *Sci. Rep.* **4**, 5767 (2014).
60. Reikowski, F. et al. Operando surface X-ray diffraction studies of structurally defined Co₃O₄ and CoOOH thin films during oxygen evolution. *ACS Catal.* **9**, 3811–3821 (2019).
61. García-Mota, M. et al. Importance of correlation in determining electrocatalytic oxygen evolution activity on cobalt oxides. *J. Phys. Chem. C* **116**, 21077–21082 (2012).
62. Monkhorst, H. J. & Pack, J. D. Special points for Brillouin-zone integrations. *Phys. Rev. B* **13**, 5188–5192 (1976).
63. Mathew, K., Sundararaman, R., Letchworth-Weaver, K., Arias, T. & Hennig, R. G. Implicit solvation model for density-functional study of nanocrystal surfaces and reaction pathways. *J. Chem. Phys.* **140**, 084106 (2014).

Acknowledgements

We acknowledge the National Research Foundation of Korea (NRF) grants funded by the Korean government (MSIT) (no. NRF-2018M1A2A2063868, no. NRF-2019R1A4A1025848, no. NRF-2019M3E6A1065102, no. 2015M3D1A1070639, and no. NRF-2018R1C1B6006854). J. Lim also acknowledges support from the Samsung Science and Technology Foundation under project no. SRFC-MA2002-04. We express thanks to the staff and crew of the Seoul National University Electron Microscopy Facility (NCIRF), Research Institute of Advanced Materials (RIAM), the Institute of Applied Physics of Seoul National University and the Seoul National University Co-operative Flexible Transformative (SOFT) Foundry. J.W. gratefully acknowledges the SNU Science Fellowship (NRF-2019R1A6A1A10073437) funded by the Korean government (MSIT).

Author contributions

J.W. contributed to the experimental planning, sample preparation, electrochemical experiments, synchrotron-based experiments, data analysis and manuscript preparation.

S.-J.K., Y.G., H.S. and Hyungjun Kim conducted the DFT calculations and contributed to manuscript preparation. S.C., K.H.C., J.K. and M.G.K. supported the operando XAFS and ex situ sXAS experiments. J.H. and S.-P.C. conducted the TEM/STEM analysis. S.J. and Hwiho Kim contributed to the ICP-MS and XPS tests. Q.L. and W.Y. performed the RIXS experiments. J. Liu., F.C., X.L. and S.Y. assisted with the sample preparation, electrochemical test, data acquisition and analysis. J. Lim. supervised the project and contributed to the experimental planning, data analysis and manuscript preparation. All authors reviewed and commented on the manuscript before publication.

Competing interests

The authors declare no competing interests.

Additional information

Supplementary information The online version contains supplementary material available at <https://doi.org/10.1038/s41929-021-00578-1>.

Correspondence and requests for materials should be addressed to J.W., S.Y., H.K. or J.L.

Peer review information *Nature Catalysis* thanks Marcel Risch, Kirsten Winther and the other, anonymous, reviewer(s) for their contribution to the peer review of this work.

Reprints and permissions information is available at www.nature.com/reprints.

Publisher's note Springer Nature remains neutral with regard to jurisdictional claims in published maps and institutional affiliations.

© The Author(s), under exclusive licence to Springer Nature Limited 2021